SUPPLEMENTARY INFORMATION FOR

Boosting C_2H_4 electrosynthesis from CO_2 via Cu-nanoparticle-anchored carbon aerogels as tubular gas-flow-through electrodes

Yu Huang [a, #], Ruiquan Yu [a, #], Hua Zhong [a], Ming Gao [a], Hao Lin [a], Xiao-yan Li [a,b], Lin Lin [a,*]

[a] *Shenzhen Engineering Research Laboratory for Sludge and Food Waste Treatment and Resource Recovery, Tsinghua Shenzhen International Graduate School, Tsinghua University, Shenzhen 518055, China*

[b] *Department of Civil Engineering, The University of Hong Kong, Pokfulam, Hong Kong, China*

[#] Authors contributed equally

*Corresponding author: linlin00@sz.tsinghua.edu.cn (L. Lin)

Supplementary Information contains: 5 Texts, 6 Figures and 2 Tables,

Text S1. Chemicals and materials

N, N-dimethylformamide (DMF, ≥99.5%), Cupric acetate anhydrous ($C_4H_6CuO_4$, ≥98%) were purchased from the Shanghai Aladdin Biological Technology Co., Ltd. Polyacrylonitrile (PAN, average MW 150,000), Sodium bicarbonate ($NaHCO_3$, 99.9%), Sodium hydroxide (NaOH, 99%) and Isopropyl alcohol (C_3H_8O, ≥99.5%) were purchased from Shanghai Macklin Biochemical Co., Ltd. The anion exchange membrane (FAA-3-PK-130) and Pt foil (20×20×1 mm) were purchased from Suzhou Sinero Technology Co., Ltd. The carbon dioxide (99.999% purity) and nitrogen (99.999% purity) were purchased from Shenzhen Huatepeng Gas Company. Ultra-pure deionized water (18.2 MΩ·cm) used in all the experiments was obtained from the Milli-Q® Direct 8 system. All reagents were used without further purification.

Text S2. Fabrication of Cu-SA-TCA and Cu-NP-TCA

PAN of 1 g was dissolved into DMF of 10 g forming a homogeneous colloidal solution. After adding 0.1/0.5 g (for single atom and nanoparticles) of $Cu(CH_3COO)_2$, the solution was magnetically stirred for 48 h at 50 °C to form a transparent solution. Then the solution was injected into a syringe pump and ejected at a constant rate of 0.01 mL/min and an applied voltage of 15 kV. The distance between the needle tip and the collector was 15 cm. Through electrospinning, a nanostructure fiber composed of carbon and copper precursors was produced. The obtained nanofiber was directly soaked into 10% iso-propyl alcohol solutions (in water), then transferred into a cylinder vessel model and dried in freeze-drying for 72 h. The nanofiber

aerogel is stabilized at 250°C in air for 2 hours, then carbonized at 900°C at 5°C min^{-1} under nitrogen for 2 hours, forming the Cu-SA-TCA/Cu-NP-TCA.

Text S3. Material **c**haracterizations

The XRD patterns of the samples were collected using a Shimadzu XRD-6000 diffractometer (40 kV, 40 mA, graphite-filtered Cu Kα radiation, λ = 0.15418 nm). SEM performed on a Zeiss Supra 55 was used to obtaining the microstructure morphology of the catalysts. HRTEM photographs were taken using a JEOL JEM-2100 microscope. XPS was employed using a Thermo Scientific K-Alpha to assess the chemical state of the catalysts. Cu X-ray absorption spectra (XAS) measurement was performed at the beamline 1W1B of the Beijing Synchrotron Radiation Facility (BSRF), Institute of High Energy Physics (IHEP), Chinese Academy of Sciences (CAS). The X-ray absorption near edge structure (XANES) experiments were performed at the BL12B-A beamline in the National Synchrotron Radiation Laboratory (NSRL), University of Science and Technology of China (USTC), Hefei, P. R. China. The in situ attenuated total reflection Fourier transform infrared (ATR-FTIR) spectroscopy measurements were conducted using a custom electrochemical cell equipped with a Ge internal reflection element. To prepare the working electrode, the as-synthesized samples were ground into fine powders and drop-cast onto a glassy carbon electrode. A Pt wire and an Ag/AgCl electrode were employed as the counter and reference electrodes, respectively. The electrochemical tests were performed at from open circuit potential (OCP) to −2.0 V vs. RHE in 1 M KOH. Prior to the spectral acquisition, the electrolyte was first purged with Ar for 30

min to remove dissolved oxygen, followed by continuous CO_2 bubbling at a flow rate of ~30 mL·min^{-1} for another 30 min to reach saturation. A background IR spectrum was subsequently recorded under open-circuit conditions. Finally, upon applying the fixed cathodic potential under continuous CO_2 flow, in-situ spectra were continuously acquired at a resolution of 4 cm^{-1}. Each final spectrum was obtained by co-adding 32 interferograms over a collection period of 30 s.

Text S4. Electrochemical measurements

All electrochemical measurements in this study were conducted on a custom coaxial three electrode system using the electrochemical workstation (AUTOLAB PGSTAT302N). In the cylindrical cell, the work electrode was the TCA assembled with a porous stone diffuser, and the Hg/HgO (saturated with 3.5 M KCl) and a cylindrical Pt mesh were used as the reference electrode and counter electrode, respectively. An anion exchange membrane (FAA-3-PK-130) was adopted to separate the reactor into an inner and an outer compartment. All potentials were referenced to reversible hydrogen electrode (RHE) with the equation of E (vs. RHE) = E (Hg/HgO) + 0.098 V + 0.059 V × pH. The CO_2-saturated 0.5 M $NaHCO_3$ or 1 M KOH was used as the electrolyte and the amount of electrolyte in each compartment was 30 mL. Prior to the measurement for CO_2RR performance, the electrolyte was purified with high purity CO_2 (99.999%) for at least 40 min. The electrochemical active surface area (ECSA) was determined by measuring double-layer capacitance (C_{dl}) using Cyclic Voltammetry (CV) in a non-Faradaic potential window (from 0.88 to 0.98 V vs. RHE) at various scan rates of 40, 60, 80, 100, and

120 mV s^{-1}. Electrochemical impedance spectroscopy (EIS) measurements were performed in a frequency range from 10^6 to 10^{-2} Hz with an amplitude of 5 mV at −1.0 V vs. RHE. The gaseous products were identified and quantified in real time from the cathodic part of the CO_2RR reactor by online gas chromatography (GC, model iGC 7200A) equipped with flame ionization detectors (FIDs for carbon product detection) and a thermal conductivity detector (TCD for H_2 detection). The gas products from the CO_2RR reactor were injected into the GC at regular intervals of 20 min during continuous 1 h chronoamperometry measurements. The actual amounts of each gas (H_2, CO and hydrocarbons) produced during the chronoamperometric test were calculated from the peak area of the GC spectrum with conversion factors based on calibration of standard gases. The liquid products were analyzed by using NMR spectroscopy (Bruker AVANCE AVIII 400) with dimethyl sulfoxide as an internal standard. Specifically, 500 μL of the reacted electrolyte, 100 μL of D_2O and 10 μL dimethyl sulfoxide solution (10 μL of dimethyl sulfoxide in 5 mL of deionized water) were mixed together. The one-dimensional 1H spectrum was measured with the water suppression method.

Text S5. Finite element modeling

The electric potential distribution and current density profiles within different electrode configurations were modeled via Primary Current Distribution. Two distinct geometric models were constructed to represent the experimental setups: the proposed coaxial cell, characterized by radial symmetry, and the conventional planar H-type cell. To focus on the geometric

influence on the electric field, the primary current distribution was calculated by solving the Equation (1)-(3) within the electrolyte domain, assuming constant ionic conductivity. This computational approach allows for a quantitative assessment of the ohmic voltage drop and the homogeneity of electric field lines across the working electrode surface.

$$\mathrm{i}_s = -\sigma_s \nabla \phi_s, \nabla \cdot \mathrm{i}_s = Q_s \quad (1)$$

$$\mathrm{i}_l = -\sigma_l \nabla \phi_l, \nabla \cdot \mathrm{i}_l = Q_l \quad (2)$$

$$\phi_s - \phi_l = E_{\mathrm{eq}} \quad (3)$$

Where σ denotes the conductivity. ϕrepresents electric potential. s and l represents the electrode and electrolyte, respectively. E_{eq} represents the equilibrium potential for reaction.

To simulate the CO_2 mass transport within the micro-channels of the aerogel, a simplified 2D rectangular axisymmetric model with a length of 10 μm and a radius of 1 μm was designed to represent the single-pore environment. Transport of Diluted Species coupled with Laminar Flow and Stationary study were used for this modeling. The side wall of the pore was defined as the active flux boundary where CO_2 is consumed. To assess the impact of the reactant phase on transport efficiency, two distinct operating modes were investigated:

(I) Liquid-diffusion mode: The pore domain was defined as liquid water with a CO_2 diffusion coefficient (D, 2e−9 m^2/s). In this scenario, the reaction flux is governed by Equation (4), representing a process limited by liquid-phase mass transfer and intrinsic kinetics.

(II) Gas-flow-through mode: A laminar flow was defined with a constant inlet velocity (0.1 m/s) boundary condition to simulate pressure-driven CO_2 supply. The corresponding velocity profile was coupled to the similar the convection-diffusion equation with liquid-

diffusion mode.

$$J = -k_{react} \cdot c \quad (4)$$

where J represents the local molar flux of CO_2 consumption. k_{react} (0.01 m/s) is the intrinsic electrochemical reaction rate constant, assumed to be sufficiently large to simulate the mass-transport-limited regime. c (33 mol/m^3) denotes the maximum soluble CO_2 concentration in the bulk liquid phase. The model was solved using a stationary solver with physics-controlled fine meshing to ensure numerical stability and accuracy.

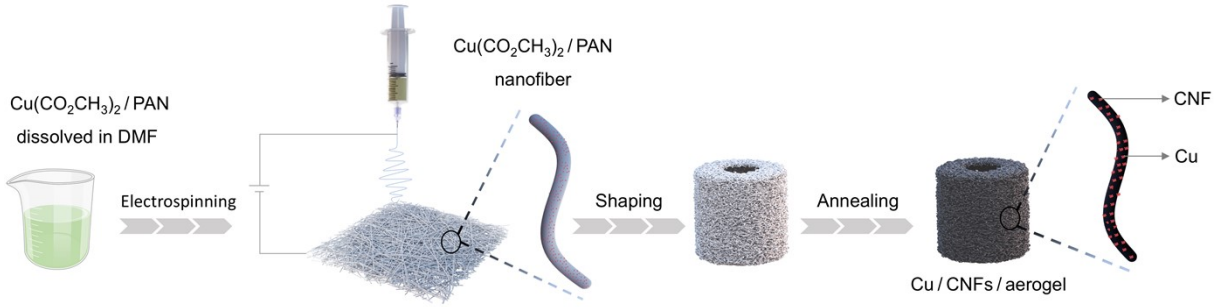

Fig. S1. Schematic illustration of (Cu-)TCA fabrication.

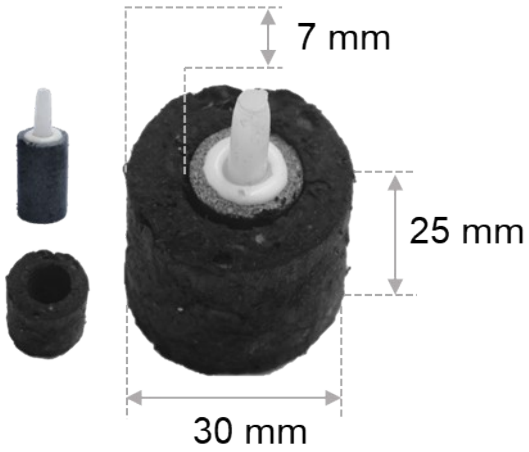

Fig. S2. Digital photos of the TCA electrodes.

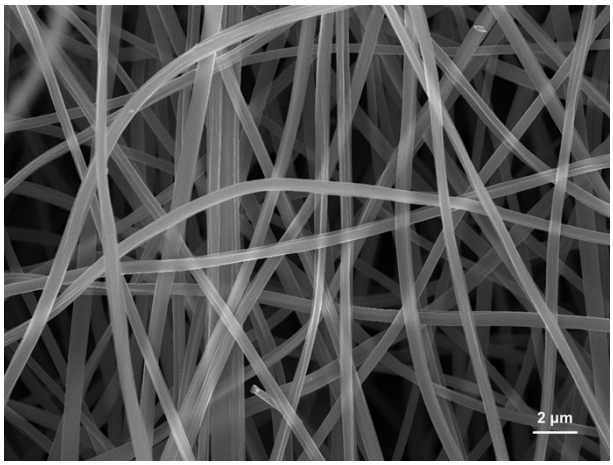

Fig. S3. SEM image of TCA.

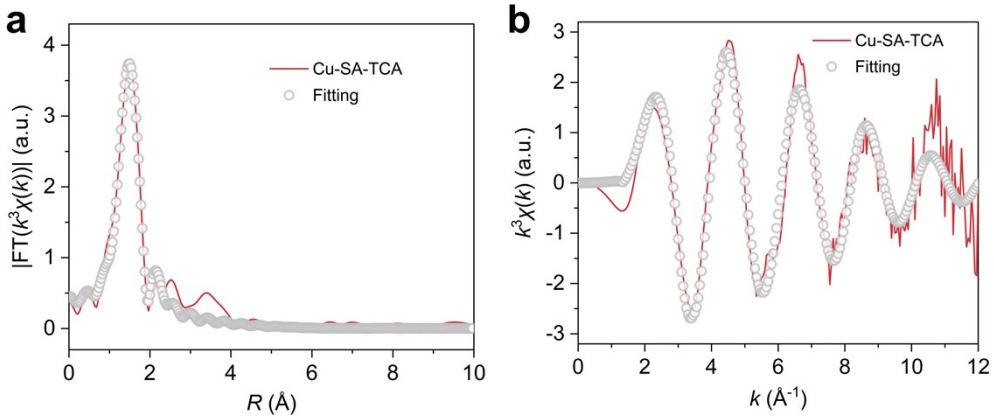

Fig. S4. EXAFS fitting results of Cu-SA-TCA. (a) The k^3-weighted FT EXAFS spectra in R-space, (b) The EXAFS oscillation signals in k-space.

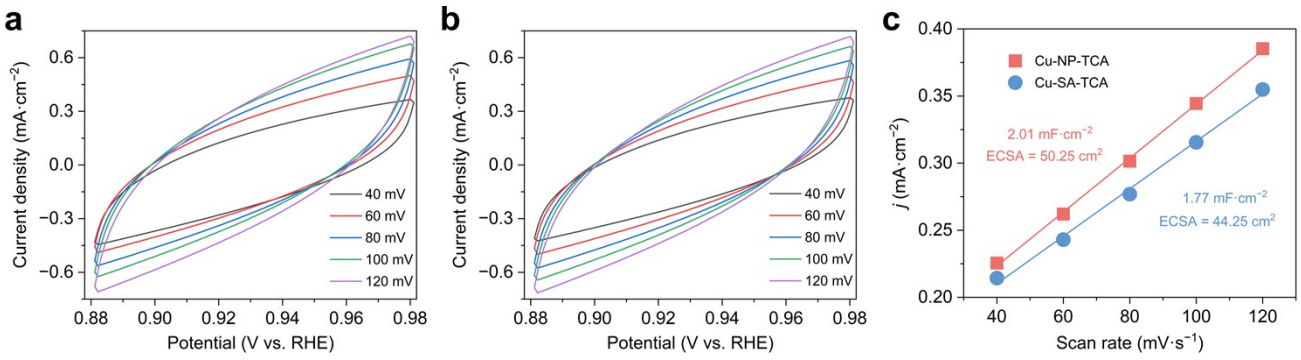

Fig. S5. CV measurements and for determining the ECSA for Cu-NP-TCA and Cu-SA-TCA. (a) CV curves measured from 0.88 to 0.98 V vs. RHE at scan rates of 40, 60, 80, 100, and 120 mV s^{-1}. (b) The non-Faradaic current density measured at 0.93 V vs. RHE as a function of the scan rate. The absolute value of the slope is taken as the double-layer capacitance (C_{dl}) of the electrode. The ECSA is calculated by the equation: ECSA = C_{dl} / C_s, where C_s is taken as 40 μF·cm^{-2} in this study, which is an average value for carbon materials).[1]

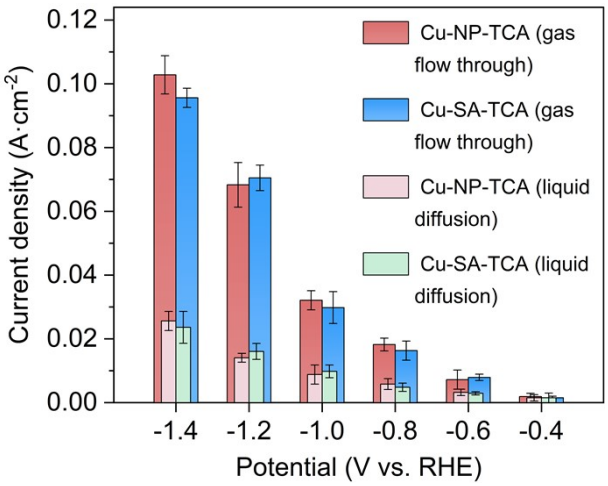

153

154 **Fig. S6.** Steady-state current densities of the Cu-NP-TCA and Cu-SA-TCA electrodes operating

155 under gas-flow-through mode versus conventional liquid diffusion mode across a potential

156 range of −0.4 V to −1.4 V vs. RHE.

157

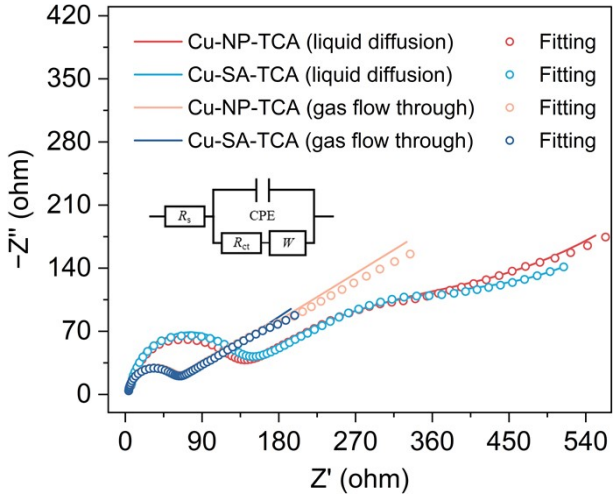

158

159 **Fig. S7.** Nyquist plots and of Cu-NP-TCA and Cu-SA-TCA under CO_2 bubbling and flowing

160 through conditions and corresponding fitted curves based on the equivalent circuit model (the

161 inset).

162

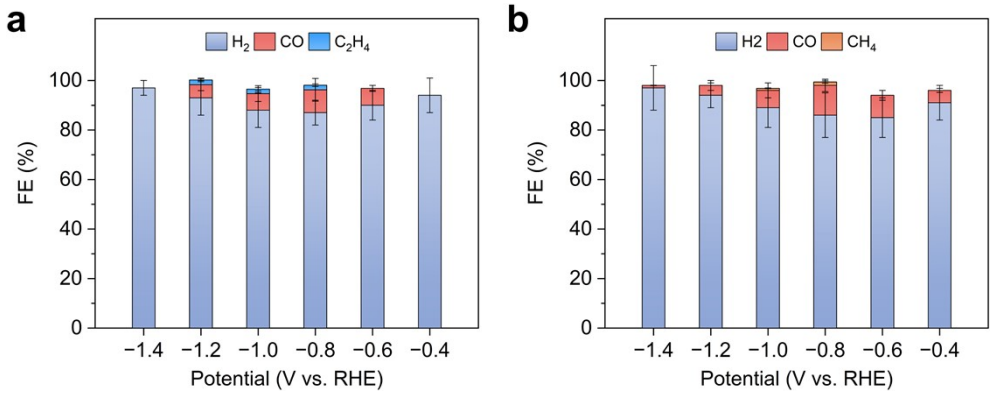

Fig. S8. FE for detected carbonaceous products of (a) Cu-NP-TCA and (b) Cu-NP-TCA in neutral conditions operating in conventional gas diffusion mode.

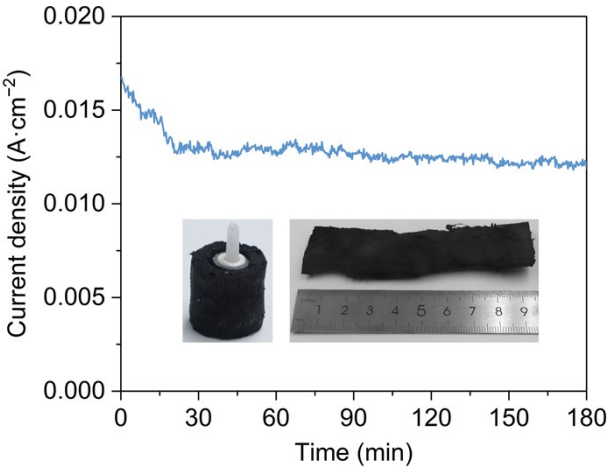

Fig. S9. The chronoamperometry curve of TCA during 3 h CO_2 penetration at with a flow rate of 50 sccm and the inset shows digital photos of TCA after operation.

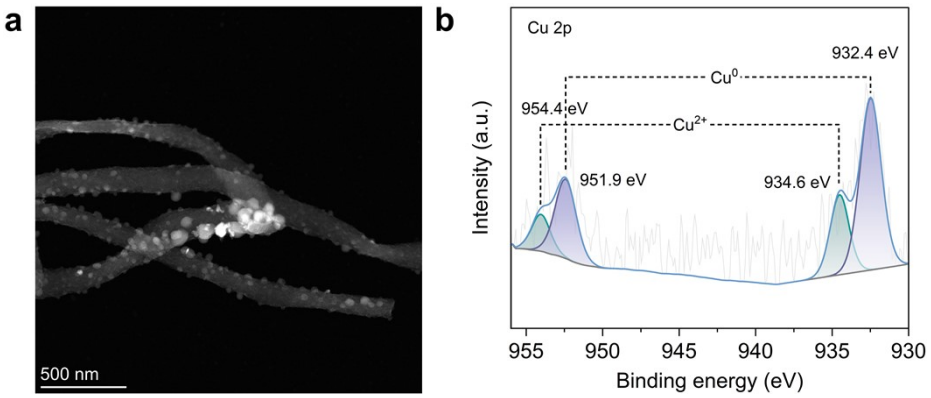

Fig. S10. (a) HRTEM image and (b) Cu 2p XPS spectrum of the used Cu-NP-TCA.

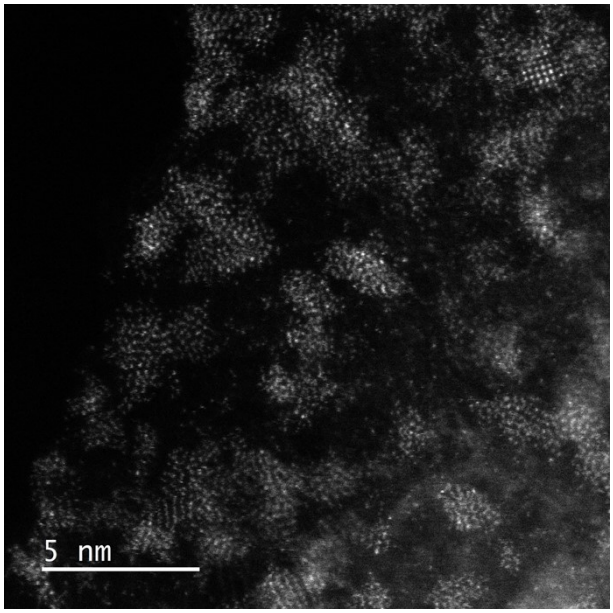

Fig. S11. HAADF-STEM image of the used Cu-SA-TCA.

Table S1. EXAFS fitting parameters at the Cu K-edge for Cu-SA-TCA.

Samples	Shell	CN	R (Å)	σ^2 (Å^2)	ΔE_0 (eV)	R factor (%)
Cu-SA-TCA	Cu-N	3.9	1.94	0.009	−2.1	0.02

Note: CN, coordination number; R, distance between absorber and backscatter atoms; σ^2, Debye-Waller factor to account for both thermal and structural disorders; ΔE_0, inner potential correction; R factor indicates the goodness of the fit.

Table S2. Impedance parameters deduced from the equivalent circuit model of Nyquist plot.

		R_s/Ω	R_{ct}/Ω	R_W/Ω (1 Hz)
Cu-NP-TCA	Liquid diffusion	3.68	105	633
	Gas flow through	4.32	35.4	345
Cu-SA-TCA	Liquid diffusion	4.07	114	752
	Gas flow through	4.08	39.5	423

Table S3. Comparison of C_2H_4 production performance of Cu-NP-TCA with reported literatures.

Materials	Potential (V vs. RHE)	Current density ($mA \cdot cm^{-2}$)	FE (%)	Ref.
Cu-NP-TCA	−1.0V	35	29	This work
Cu_g-PCN	−1.1V	7.5	20	[2]
Cu-C-N900	−1.4V	25	24.8	[3]
PACuDBC-2	−1.1V	35	12	[4]
Cu10-Sn	−1.29V	48	12	[5]
Cavity cubes	−1.3V	16	5.75	[6]
Cu_2O@CM	−1.1V	15	28.7	[7]
Cu90Ag10	-	40	33	[8]
Cu NPs/Ni–N–C-2	−0.9V	11.7	14.27	[9]
Cu/C_S	−1.5V	10	14.07	[10]
Gd-CuO-w	−1.2V	20.8	24	[11]
$Ag_{85}Cu_{15}$ aerogel	−1.0V	7.5	12.9	[12]
Pt1Ni1@Cu1	−1.2V	24	30.9	[13]
CuO-Sn1%	−1.5V	20.8	17.7	[14]
Cu-10/NC	−1.1V	6.5	30.3	[15]
electrodeposited Cu_2O	−1.13V	9.6	26	[16]
Cu mesocrystals	−0.99V	10	27.2	[17]
Ag@Cu Np	−1.2V	20.4	41.3	[18]

Reference

1. H. Fei, J. Dong, M. J. Arellano-Jiménez, G. Ye, N. Dong Kim, E. L. G. Samuel, Z. Peng, Z. Zhu, F. Qin, J. Bao, M. J. Yacaman, P. M. Ajayan, D. Chen and J. M. Tour, *Nature Communications*, 2015, **6**, 8668.
2. H. G. El-Aqapa, G. E. Khedr, I. M. Badawy, A. M. Agour, A. M. Abdelmohsen and N. K. Allam, *Journal of Materials Chemistry A*, 2025, **13**, 7091-7095.
3. A. Guan, Z. Chen, Y. Quan, C. Peng, Z. Wang, T.-K. Sham, C. Yang, Y. Ji, L. Qian, X. Xu and G. Zheng, *ACS Energy Letters*, 2020, **5**, 1044-1053.
4. S. Wei, X. Jiang, C. He, S. Wang, Q. Hu, X. Chai, X. Ren, H. Yang and C. He, *Journal of Materials Chemistry A*, 2022, **10**, 6187-6192.
5. H. Wang, F. Zhang, Y. Li, Y. Pang, X. Zhao, Z. Song, W. Wang, J. Sun and Y. Mao, *J Colloid Interface Sci*, 2025, **678**, 506-514.
6. G. Cao, X. Cao, M. Shan, M. Li, X. Zhu, J. Han, Q. Ge and H. Wang, *Journal of Solid State Electrochemistry*, 2022, **26**, 1527-1540.
7. S. Min, Z. Wang, X. Xu, J. He, M. Sun, W. Lin and L. Kang, *Applied Surface Science*, 2024, **663**.
8. Y. E. Jeon, Y. N. Ko, J. Kim, H. Choi, W. Lee, Y. E. Kim, D. Lee, H. Y. Kim and K. T. Park, *Journal of Industrial and Engineering Chemistry*, 2022, **116**, 191-198.
9. L.-L. Zhang, K.-A. Wang, G.-R. Zhu, J.-Y. Shi and H.-B. Zhu, *Journal of Materials Science*, 2023, **58**, 17200-17210.
10. H. Noh, Y. Park, A. Bhadouria and B. M. Tackett, *Journal of Catalysis*, 2024, **437**.
11. Z. Cao, Z. Chen, H. Sun, S. Yao, Z. Liu, F. Li, X. Yang, W. Zhou, J. Fan, H. Wang and L. Liu, *Journal of Materials Chemistry A*, 2024, **12**, 29165-29173.
12. J. Wang, J. Soo‐Hyun Park, A. Imam, Z. Yu, Z. Fang, M. Noroozifar and H. B. Kraatz, *ChemCatChem*, 2024, **16**.
13. Y. Xiao, Y. Yang, W. Liu and J. Liu, *Journal of Materials Chemistry A*, 2025, **13**, 26812-26822.
14. H. Chuai, S. Liu, Z. Liang, H. Liu, Q. Zhao and S. Zhang, *Chemical Engineering Journal*, 2025, **518**.
15. J. Han, J. Ma, J. Zhou, X. Chen, Z. Wan and Y. Zhao, *Applied Surface Science*, 2023, **609**.
16. D. Kim, S. Lee, J. D. Ocon, B. Jeong, J. K. Lee and J. Lee, *Phys Chem Chem Phys*, 2015, **17**, 824-830.
17. C. S. Chen, A. D. Handoko, J. H. Wan, L. Ma, D. Ren and B. S. Yeo, *Catalysis Science & Technology*, 2015, **5**, 161-168.
18. L. Hou, J. Han, C. Wang, Y. Zhang, Y. Wang, Z. Bai, Y. Gu, Y. Gao and X. Yan, *Inorganic Chemistry Frontiers*, 2020, **7**, 2097-2106.